

Triage of the *Gaia* astrometric orbits. I. A sample of binaries with probable compact companions

S. Shahaf,^{1*} D. Bashi,² T. Mazeh,² S. Faigler,² F. Arenou,³ K. El-Badry,^{4,5,6} and H. W. Rix⁶

¹*Department of Particle Physics and Astrophysics, Weizmann Institute of Science, Rehovot 7610001, Israel*

²*School of Physics and Astronomy, Tel Aviv University, Tel Aviv, 6997801, Israel*

³*GEPI, Observatoire de Paris, Université PSL, CNRS, 5 Place Jules Janssen, 92190 Meudon, France*

⁴*Center for Astrophysics | Harvard & Smithsonian, 60 Garden Street, Cambridge, MA 02138, USA*

⁵*Harvard Society of Fellows, 78 Mount Auburn Street, Cambridge, MA 02138*

⁶*Max-Planck Institute for Astronomy, Königstuhl 17, D-69117 Heidelberg, Germany*

Accepted XXX. Received YYY; in original form ZZZ

ABSTRACT

In preparation for the release of the astrometric orbits of *Gaia*, Shahaf et al. (2019) proposed a triage technique to identify astrometric binaries with compact companions based on their astrometric semi-major axis, parallax, and primary mass. The technique requires the knowledge of the appropriate mass-luminosity relation to rule out single or close-binary main-sequence companions. The recent publication of the *Gaia* DR3 astrometric orbits used a schematic version of this approach, identifying 735 astrometric binaries that might have compact companions. In this communication, we return to the triage of the DR3 astrometric binaries with more careful analysis, estimating the probability for its astrometric secondary to be a compact object or a main-sequence close binary. We compile a sample of 177 systems with highly-probable non-luminous massive companions, which is smaller but cleaner than the sample reported in *Gaia* DR3. The new sample includes 8 candidates to be black-hole systems with compact-object masses larger than $2.4 M_{\odot}$. The orbital-eccentricity–secondary-mass diagram of the other 169 systems suggests a tentative separation between the white-dwarf and the neutron-star binaries. Most white-dwarf binaries are characterized by small eccentricities of about 0.1 and masses of $0.6 M_{\odot}$, while the neutron star binaries display typical eccentricities of 0.4 and masses of $1.3 M_{\odot}$.

Key words: astrometry – binaries: general – stars: white dwarfs – stars: neutron – stars: black holes

1 INTRODUCTION

The population of binaries with white-dwarf, neutron-star, or black-hole companions is of great interest. It sheds light on the properties of the binaries for which the more massive primary component completed its main-sequence (MS) phase and on the dramatic processes accompanying the transition into a compact object (e.g., Heger et al. 2003; Cerda-Duran & Elias-Rosa 2018). Astrometry is an important tool to study this population, as it is sensitive to binaries with orbital periods of the order of a few years, depending on the binary distance, which corresponds to orbital separations to which other techniques, spectroscopy or photometry, are less sensitive (e.g., Jorissen & Frankowski 2008). Furthermore, unlike spectroscopic binaries for which the orbital inclination is not known, the compact-object mass in astrometric binaries can be determined, and the three types of compact objects can, in principle, be distinguished (e.g., Halbwachs et al. 2022).

The *Gaia* astrometric space mission (Gaia Collaboration et al. 2016) provides a promising detection channel, as it is expected to detect an unprecedentedly large number of astrometric binaries. For example, theoretical studies predict that the *Gaia* mission carries the potential of discovering hundreds of binaries with non-interacting

black-holes in orbital periods $\lesssim 5$ years (e.g., Breivik et al. 2017; Mashian & Loeb 2017; Yamaguchi et al. 2018; Janssens et al. 2022; Chawla et al. 2022). Neutron stars and white dwarfs should be even more frequent (e.g., Fryer et al. 2012). Note, however, that the stringent selection criteria imposed on the DR3 sample of astrometric binaries (see Halbwachs et al. 2022), designed to reduce the contamination of the astrometric catalogue by spurious signals, probably excluded many of these systems, impairing the detection of the compact objects.

In preparation for the release of the astrometric orbits of *Gaia*, Shahaf, Mazeh, Faigler & Holl (2019) proposed a triage technique to identify astrometric binaries that have compact companions based on their derived semi-major axis, parallax, orbital period and the estimated primary mass. The technique requires the knowledge of the proper mass-luminosity relation (MLR) to rule out a single or a close-binary MS companion. Indeed, the DR3 binary release (Gaia Collaboration, Arenou et al. 2022, hereafter *NSS* — Non-Single Stars) used a schematic version of this approach, with the MLR of Pecaut & Mamajek (2013), to identify 735 astrometric binaries with compact companions (see also Andrews et al. 2019; Andrew et al. 2022, for a different approach).

In this communication, we return to the triage of the DR3 astrometric binaries with a more careful analysis that uses a more conservative MLR to identify compact-secondary binaries based on

* E-mail: sahar.shahaf@weizmann.ac.il

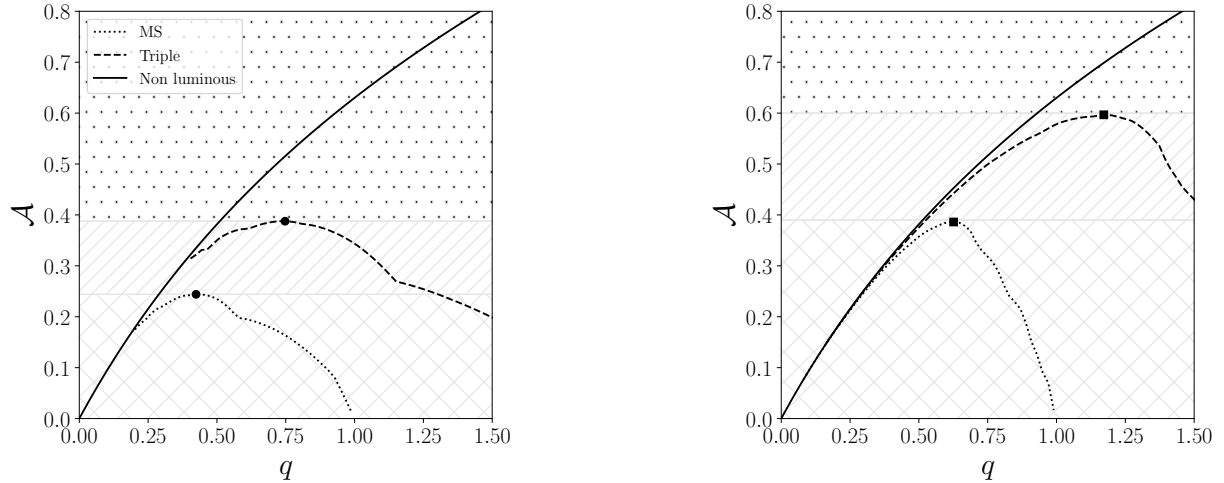


Figure 1. Expected AMRF curves as a function of q for primaries of $0.4 M_{\odot}$ (left) and $1.0 M_{\odot}$ (right), based on the empirical MLR of Pecaut & Mamajek (2013) for the *Gaia* G band. Lines represent three limiting cases for an astrometric companion: a single MS secondary is shown as a dotted line; a close equal-mass MS binary, as the astrometric companion, appears as a dashed line, and a non-luminous companion is plotted as a solid line. No binary can exist below the dotted line. All triple systems have to reside between dashed and dotted lines. Binaries above the dashed lines must be compact objects. Points mark the maximum \mathcal{A} for single and close-pair MS companions. We do not know the actual mass ratio, so the maximum points divide the possible \mathcal{A} values into three ranges.

a suit of MIST isochrone grids.¹ We derive a less contaminated catalogue of compact companions, identifying astrometric binaries with white-dwarf, neutron-star or black-holes companions.

The paper is structured as follows: In Section 2 we briefly describe our astrometric triage scheme and discuss the effect of stellar age and composition on this technique. In Section 3 we present the triage of *Gaia* DR3 binaries, provide a list of class-membership probabilities, and compile a sample of systems that are very likely to host a compact object in Section 4. In Section 5 we show some of the emerging properties of our compact-object sample. Finally, in Section 6 we briefly discuss the sample and preliminary findings and propose some ideas for future work.

2 ASTROMETRIC TRIAGE

In this section, we re-discuss the astrometric triage introduced by Shahaf et al. (2019), with a focus on using the appropriate MLR for MS stars.

Consider an astrometric binary with an angular semi-major axis α_0 . For an unresolved binary, α_0 reflects the motion of the centre-of-light around the binary centre-of-mass. In cases where the more luminous primary star is significantly brighter than its secondary companion, the photo centre of the system is located near the primary star’s position. This could happen, for example, if the secondary is a faint sub-stellar companion or a compact object. On the other hand, if both components are luminous, the photo centre is located near the centre-of-mass of the binary, up to a point where no astrometric orbit can be detected.

Shahaf et al. (2019) presented the astrometric mass ratio function (AMRF),

$$\mathcal{A} \equiv \frac{\alpha_0}{\varpi} \left(\frac{M_1}{M_{\odot}} \right)^{-1/3} \left(\frac{P}{\text{yr}} \right)^{-2/3}, \quad (1)$$

where P and ϖ are the orbital period and parallax, and M_1 is the primary mass. \mathcal{A} can be determined for every astrometric binary for which M_1 is known.

The unknown mass ratio $q = M_2/M_1$ is linked to AMRF via

$$\mathcal{A} = \frac{q}{(1+q)^{2/3}} \left(1 - \frac{\mathcal{S}(1+q)}{q(1+\mathcal{S})} \right), \quad (2)$$

where $\mathcal{S} = F_2/F_1$ is the luminosity ratio between the two components. Shahaf et al. (2019) showed that whenever the luminosity ratio of the two possible MS stars can be expressed as a function of the mass ratio, $\mathcal{S}(q)$, one is able to place some constraints on the nature and properties of the faint companion in the binary system.

In the case of a compact-object secondary, for which $\mathcal{S} = 0$, the mass ratio, and hence the secondary mass, can be derived. The estimated mass may, in many cases, constrain the compact object’s nature. However, this can only be done if we rule out the possibility of a single MS secondary or a companion who is by itself a close MS binary. If \mathcal{S} is unknown, a lower limit for the mass of the companion, $M_{2,\text{min}}$, can be derived by assuming it is non-luminous. This is described in Appendix A.

2.1 AMRF classification

To illustrate the triage approach, we plot in Figure 1 two theoretical AMRF curves as a function of the mass ratio q , for 0.4 and $1.0 M_{\odot}$ MS primary stars. The dotted (lower) curves in the two panels present binaries with a single MS secondary; the dashed (upper) curves triple systems, with a close equal-mass MS binary as the astrometric secondary; and the solid curves binaries with a non-luminous companion. The dotted and dashed lines were derived with the *Gaia* G-band MLR of Pecaut & Mamajek (2013).

Note that binaries with MS companions have to reside on the lower dotted curves, with a position that depends on the mass ratio of the astrometric binary. Triple systems with close-binary MS companions could be located anywhere below the upper dashed line, depending on the mass ratio of the close binary. Only triple systems with equal-

¹ MESA Isochrones & Stellar Tracks. See waps.cfa.harvard.edu/MIST/.

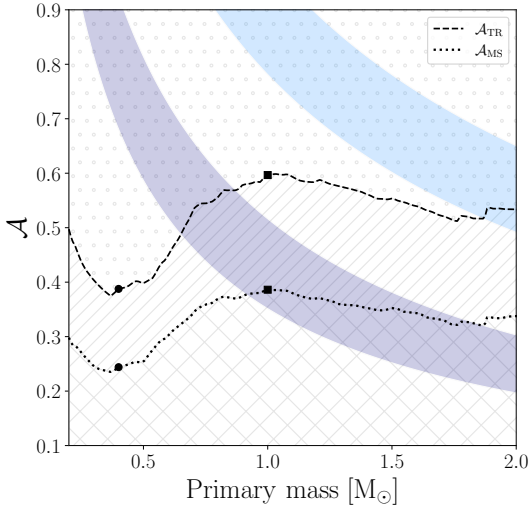


Figure 2. Maximum \mathcal{A} for an MS secondary (dotted line) and an MS close-binary companion (dashed line) as a function of primary mass, based on Pecaut & Mamajek (2013) observed MLR. Black circles and squares show the maximum values of Fig. 1. Purple and light-blue stripes illustrate the expected \mathcal{A} of white dwarfs, at 0.45–0.75 M_{\odot} , and neutron stars, at 1.4–2.1 M_{\odot} companions, respectively. Note that their position does not depend on the period or the parallax of the system. The figure suggests that since some white-dwarf and most neutron-star companions are expected to reside above the corresponding maximum \mathcal{A} , they can be identified as such.

mass close-binary companions have to be on the upper dashed line, with a position that depends on the wide-binary mass ratio. Binaries with compact companions have to reside on the continuous curve.

The AMRF theoretical curves have maximal values — \mathcal{A}_{MS} for the single MS secondary and \mathcal{A}_{TR} for the triple-system curve. These values, which depend on the primary mass, are noted in the figure by dots and squares. Any wide binary with $\mathcal{A} > \mathcal{A}_{\text{TR}}$ probably has a compact companion. If the companion is a single object, the system has to reside on the continuous curve. In such a case, the companion mass can be derived from the value of \mathcal{A} .

In the general case, though, one cannot determine the value of q , even if the primary mass is known, because the luminosity of the secondary is unknown. Therefore, to identify unresolved astrometric binaries that are likely to host a compact object as their faint companion, Shahaf et al. (2019) divided the astrometric binaries into three classes, based on their measured AMRF value, \mathcal{A} :

(i) *Class-I binaries* ($\mathcal{A} < \mathcal{A}_{\text{MS}}$), where the companion is most likely a single MS star. The class-I parameter space is shown as a crisscrossed area in Figure 2.

(ii) *Class-II binaries* ($\mathcal{A}_{\text{MS}} < \mathcal{A} < \mathcal{A}_{\text{TR}}$), where the companion cannot be a single MS star, but can be either a MS close binary or a compact object. The class-II parameter space is denoted with slanted lines.

(iii) *Class-III binaries* ($\mathcal{A} > \mathcal{A}_{\text{TR}}$), where the companion cannot be a single MS star nor a close MS binary; these systems are likely to host a compact object secondary. The class-III parameter space is highlighted by small circles.

Figure 1 demonstrates that the limiting values \mathcal{A}_{MS} and \mathcal{A}_{TR} vary as a function of M_1 . Figure 2 shows the limiting AMRF values as a

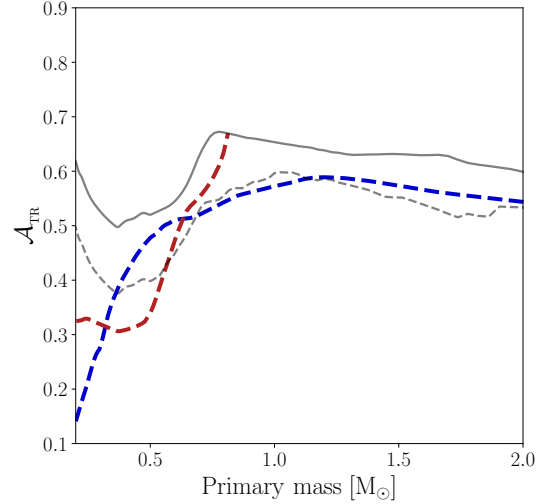


Figure 3. Impact of stellar age and metallicity on \mathcal{A}_{TR} . Class-III limiting value, \mathcal{A}_{TR} , as a function of the primary mass. Dashed red and blue lines represent the MIST-based limits for old and young stellar populations, respectively. Grey dashed line represents the limit obtained from the empirical MLR of Pecaut & Mamajek (2013) (dashed), which were used in the NSS. Grey solid line is the limiting curve adopted by this work. See Section 2.2 and Appendix B.

function of the primary mass. We added in Figure 2 purple and light-blue stripes that illustrate the expected \mathcal{A} values of white dwarfs, at 0.45–0.75 M_{\odot} , and neutron stars, at 1.4–2.1 M_{\odot} .

Note that the locations of binaries with neutron-star companions are all in the class-III region, making their identification relatively simple. However, the white-dwarf stripe is only partly above the \mathcal{A}_{TR} curve. This implies that only binaries with more massive white dwarfs can be identified, while many low-mass white dwarfs with relatively massive primaries will escape detection. We will come back to this point in an accompanying paper.

2.2 Re-consideration of class-II and class-III limits

The AMRF limits depend on the assumed MLR, which in turn depends on the age and chemical composition of the specific binary. The observed MLR of Pecaut & Mamajek (2013) used in Figure 1 and 2 is an averaged relation, taken over the distribution of ages and compositions in the Solar neighborhood. While this relation can properly describe the population of stars in the field, this is not necessarily the case when considering two stars in a particular binary system. Assuming the two stars were formed at the same time and have the same composition, their relative flux contribution follows some specific isochrone track rather than the local averaged MLR.

To demonstrate this point Figure 3 presents \mathcal{A}_{TR} for two different populations: a young population, with age of 126 Myr and $[\text{Fe}/\text{H}] = 0.5$ (a dashed-blue curve), an old population of 12.6 Gyr and $[\text{Fe}/\text{H}] = -2.5$ (dashed-red curve). To derive the first two curves we simulated a synthetic stellar population using ArtPop package²

² See the online documentation at artpop.readthedocs.io

(Greco & Danieli 2021) and the MIST isochrone grids. The figure also displays the (upper) curve of Figure 1 (dashed-gray curve), based on Pecaut & Mamajek (2013) MLR, which was used by *NSS*.

Figure 6 shows that the limit used by *NSS* often underestimates the limiting AMRF values separating between class-II and -III binaries. Therefore, we have adopted a more conservative classification curve based on the upper envelope of an ensemble of models generated over various stellar ages and metallicities. The resulting curve is plotted as a solid grey line in Figure 6. As opposed to the *NSS* classification curve, our curve provides reliable \mathcal{A}_{MS} and \mathcal{A}_{TR} curves that can be used regardless of the underlying age and metallicity of the binary. We elaborate on the derivation of the curves in Appendix B.

3 TRIAGE OF GAIA BINARIES

Equipped with a more conservative threshold for class-III binaries, we now turn to re-consider the *Gaia* astrometric binaries. First, we derive a slightly smaller sample of astrometric binaries by vetting the targets based on the reported orbital parameters. Then, we obtain the probability of each binary being in class-II or class-III, given their orbital parameters and uncertainties.

3.1 Sample selection

We first queried the *Gaia* database for astrometric binaries with MS primary stars that have mass estimate, according to the following conditions:

- (i) `nss solution type` is `Orbital` or `AstroSpectroSB1`;
- (ii) `bit index` is 8191 or 65535;
- (iii) `binary masses catalogue m1 ref` is `IsocLum`; and
- (iv) `binary masses catalogue combination method` is `Orbital+M1` or `AstroSpectroSB1+M1`.

The first two conditions require that the astrometric orbit was derived from the primary processing pipeline and has all orbital parameters fitted. The following two conditions require that a primary mass estimate exists for the system and that its primary star was classified by as an MS star in the *NSS*. This procedure left a total of 127026 targets in the sample.

We then applied the Halbwachs et al. (2022) criteria on the eccentricity error, parallax significance, $\varpi/\Delta\varpi$, and astrometric solution significance, $\alpha_0/\Delta\alpha_0$.

- (i) $\Delta e < 0.079 \ln(P/\text{day}) - 0.244$;
- (ii) $\varpi/\Delta\varpi > 20000 \cdot (P/\text{day})^{-1}$; and
- (iii) $\alpha_0/\Delta\alpha_0 > 158 \cdot (P/\text{day})^{-1/2}$.

These additional cuts, which are supposed to reduce the number of spurious orbital solutions in the sample, removed a few additional systems, and we were left with 126624 stars in a sample with a mass estimate.

Next, we opted to exclude systems with poorly constrained Thiele-Innes coefficients. A full description of these coefficients and the required formulae for using them to derive the angular semi-major axis can be found in Halbwachs et al. (2022). We required, somewhat arbitrarily, that the quadratic mean of the relative uncertainty in A , B , F , and G Thiele-Innes coefficients will be smaller than 3, namely

$$\sigma_{\text{II}}^2 \equiv \left(\frac{\Delta A}{A}\right)^2 + \left(\frac{\Delta B}{B}\right)^2 + \left(\frac{\Delta F}{F}\right)^2 + \left(\frac{\Delta G}{G}\right)^2 \leq 36. \quad (3)$$

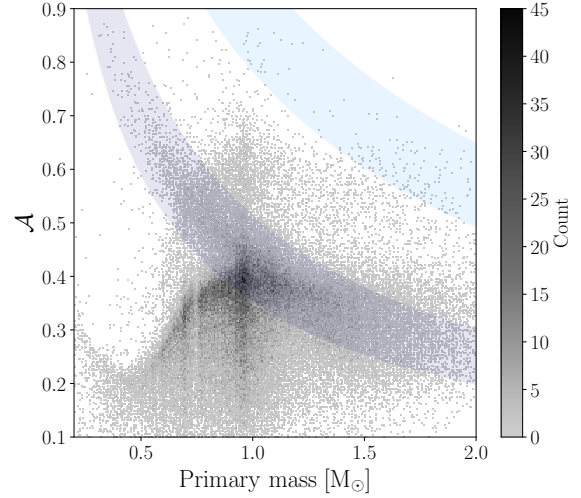


Figure 4. Density plot of the clean astrometric sample in the AMRF–primary-star mass plane, colour coded by the number of points per unit area. Purple and light-blue stripes represent the AMRF locus for typical white dwarfs and neutron stars (see Figure 2). Axes ranges were selected to clearly visualize the main locus of the distribution.

This step was taken to ensure that our classification probability estimates (see below) properly converge and left 110401 orbits in the cleaned sample.

Finally, we opted to exclude targets with orbital periods longer than the timespan of the data analyzed by *Gaia* DR3. We, therefore, removed systems with orbital periods longer than 1000 days. We were eventually left with 101380 systems in our cleaned sample, presented in Figure 4.

3.2 Classification probability

The AMRF classification of the binaries in our sample is based on the three probabilities:

$$\begin{aligned} \text{Pr I} &= \Pr(\mathcal{A} < \mathcal{A}_{\text{MS}}), \\ \text{Pr II} &\equiv \Pr(\mathcal{A}_{\text{MS}} < \mathcal{A} < \mathcal{A}_{\text{TR}}), \quad \text{and} \\ \text{Pr III} &\equiv \Pr(\mathcal{A}_{\text{TR}} < \mathcal{A}). \end{aligned} \quad (4)$$

These probabilities are evaluated using Monte-Carlo experiments. To consider the uncertainties of the orbital elements, we randomly drew $N = 10^5$ random instances of the Thiele-Innes parameters, parallax, period, eccentricity and primary mass. The sampling was performed while considering the uncertainties and covariance between the parameters, as reported in the *Gaia* catalogue.

As proposed by Shahaf et al. (2019), the values of the AMRF and primary mass determine the classification of the binary. We calculated \mathcal{A} , \mathcal{A}_{MS} , and \mathcal{A}_{TR} for each draw, and estimated the class-III probability by

$$\hat{\text{Pr III}} = \frac{r + 1}{N + 1}, \quad (5)$$

where r is the number of instances for which \mathcal{A} is larger than \mathcal{A}_{TR} (see, for example, Davison & Hinkley 1997). The class-II membership probability, $\hat{\text{Pr II}}$, was estimated similarly. For brevity, we do not use the ‘hat’ superscript in the following. We emphasize

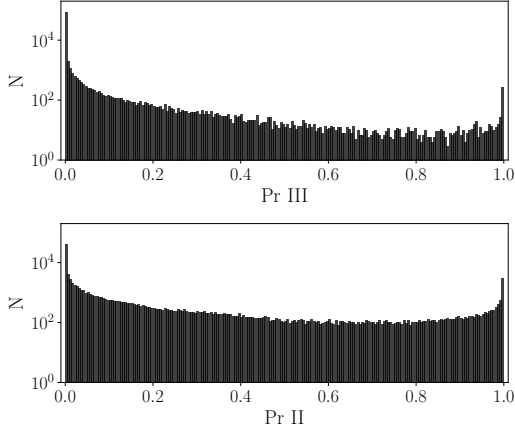


Figure 5. Histograms of derived class-III (top panel) and class-II (bottom panel) classification probabilities for the sample of 101380 binaries, reported in Table 1. Bin width in both histograms is 0.5%. Left-most and right-most bins of the Pr III (Pr II) histogram contain 87579 (41578) and 270 (3009) *Gaia* binaries, respectively.

that whenever membership probability is discussed, we refer to our bootstrap-based estimate, derived according to equation (5), as described above.

A list of the Pr II and Pr III classification probabilities for all targets in our sample is provided in Table 1. The class-I membership probability, Pr I, can be derived using the two other class probabilities, the number of Monte-Carlo samples, N , and equation (5). Histograms of the class-II and III probabilities are plotted in Figure 5, and the Pr III distribution in the AMRF–primary-mass plane in Figure 6. One can see the concentration of class-II and III above the old-age \mathcal{A}_{MS} and \mathcal{A}_{TR} curves.

Figure 6 suggests that for primary stars less massive than $\sim 0.5 M_{\odot}$, the limiting values calculated according to the MIST models tend to underestimate the transition between class-I and -II systems. This is in accord with a reported discrepancy between the empirically estimated and the theoretically expected M-dwarf radii (e.g., Morrell & Naylor 2019). As described in Appendix B, we rectified our limiting curves for primaries less massive than $0.5 M_{\odot}$, so that they were not severely affected by this discrepancy (also see Figure 3).

4 HIGHLY-PROBABLE CLASS-III SYSTEMS

We now define a sample of systems likely to host compact companions, applying the Benjamini & Hochberg (1995) false-discovery rate (FDR) approach, designed to control the expected proportion of false discoveries. In the present work context, false discoveries are systems that are wrongfully identified as class-III binaries.

We set α , the upper limit on the expectancy values of the false discovery rate, to

$$\alpha = 10\%, \quad (6)$$

which yields 177 systems in this sub-sample (class-III sample henceforth). Accordingly, only 18 ($\sim \alpha \times 177$) or fewer binaries are expected to wrongly identify class-III systems. The minimal class-III probability in the sample is 99.984%, i.e., only 16 out of the 10^5 Monte-Carlo instances fell below the \mathcal{A}_{TR} limit. A list of the binaries of this sample is given in Table 2.

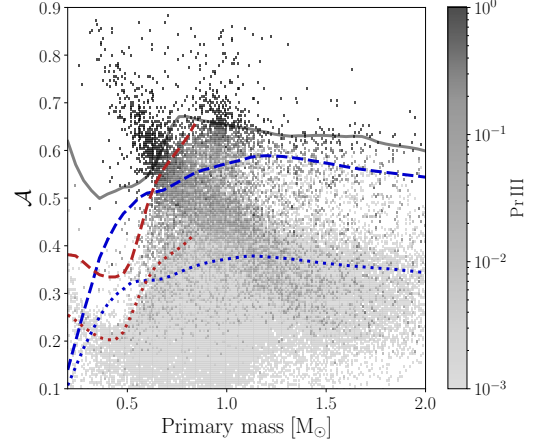


Figure 6. Average Pr III (colour coded) on the \mathcal{A} –primary-mass plane for the *Gaia* astrometric sample. Curves indicate the \mathcal{A}_{MS} and \mathcal{A}_{TR} limits for young (blue lines) and old populations (red lines), as in Figure 3. The grey line is our selected \mathcal{A}_{TR} curve (see text and Appendix B).

Source ID	G (mag)	M_1 (M_{\odot})	\mathcal{A}	$M_{2,min}$ (M_{\odot})	Pr II (%)	Pr III (%)
33711199137024	14.1	0.95	0.426(77)	0.55(13)	56.198	8.800
148953761446272	9.8	1.25	0.3850(70)	0.634(15)	0.836	0.001
301614079110400	13.0	1.01	0.580(17)	0.895(38)	75.302	24.699
858688517149056	11.0	1.22	0.196(18)	0.274(28)	0.001	0.001
1729398647131392	15.1	0.56	0.177(23)	0.112(17)	0.072	0.001
2488955023504768	14.8	0.49	0.145(18)	0.078(11)	0.001	0.001
3019435024120576	15.7	0.65	0.299(37)	0.238(35)	36.036	2.885
3205080690546176	12.9	0.85	0.397(34)	0.445(49)	19.105	0.006
3334754343120640	15.3	0.64	0.704(78)	0.75(13)	6.864	93.137
3616877859431808	13.4	0.93	0.397(17)	0.492(28)	10.752	0.001

Table 1. Probabilistic AMRF classification of the clean astrometric sample. The G-band magnitude is taken from the *Gaia* DR3 source, and the primary mass is from the binary masses table. The AMRF and its corresponding minimal secondary mass are provided with their uncertainty estimate (see Appendix A). The last two columns represent the class-II and -III probability, calculated according to Section 3.2.

Most of these systems, if their orbits are valid, contain compact secondaries. Therefore, we can then derive their masses and possibly distinguish between the white-dwarf (WD), neutron-star (NS) or black-hole (BH) companions. However, we stress the possibility that erroneous orbital fits might contaminate the sample, particularly when considering a sample of rare candidates. We therefore advocate that the validity of these orbits should be assessed externally (see the caveats discussion in Section 6).

4.1 Comparison with the NSS candidates

Gaia DR3 NSS includes a list of 735 class-III systems, while our list includes only 177 binaries. The difference emanates from:

- (i) vetting the quality of the orbital solution,
- (ii) conservatively estimating the limiting \mathcal{A}_{TR} curve, and
- (iii) setting a high-purity threshold on Pr III.

As a result of the different vetting, only 581 systems of the NSS

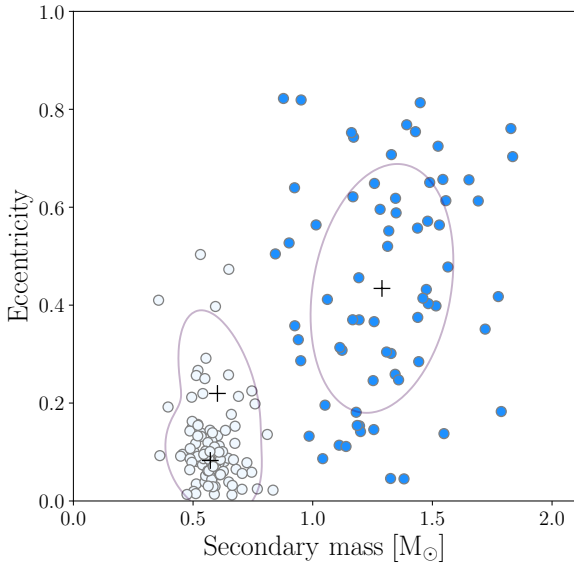


Figure 7. Orbital eccentricity versus secondary mass for the class-III sample. We set the upper boundary of the mass axis at $2.1 M_{\odot}$, for clarity. Lines represent the central regions of the fitted Gaussian mixture model (see text). Systems identified as members of the WD and NS clusters appear as white and blue circles, respectively. Lines follow a constant \ln -likelihood level of -0.5 , based on the fitted Gaussian mixture model, and highlight the main loci of the secondary-mass–eccentricity distribution. Centres of the three Gaussian components are plotted as black “+” signs.

sample are included in our list (see Section 3.1). While all these systems have $\text{Pr I} \approx 0$, only 148 were classified here as highly probable class-III systems. We attribute the difference to our conservative approach in setting the limiting classification value, \mathcal{A}_{TR} .

On the other hand, out of the 177 class-III systems classified in this study, 29 do not appear in the large DR3 catalogue. These systems were not considered by *NSS* because their significance value is smaller than 20, the limit *NSS* adopted for considering valid orbits. As explained above, we used a different limit, which we believe is more appropriate for our purpose.

4.2 Comparison with the Andrews et al. (2022) candidates

Another catalogue of 24 NS and BH candidates in *Gaia* DR3 was recently published by Andrews et al. (2022); 14 systems from this sample were included in this work (see Table 1). The remaining 10 systems were rejected in our early stage of initial sample selection (see Section 3.1).

All 14 systems shared by both samples have high class-III probabilities and appear in our class-III sample. One system, *Gaia* DR3 6328149636482597888, has a mass larger than $2.4 M_{\odot}$ and is considered a BH candidate (Table 2). The remaining 13 are NS candidates, with masses between ~ 1.2 and $\sim 1.8 M_{\odot}$.

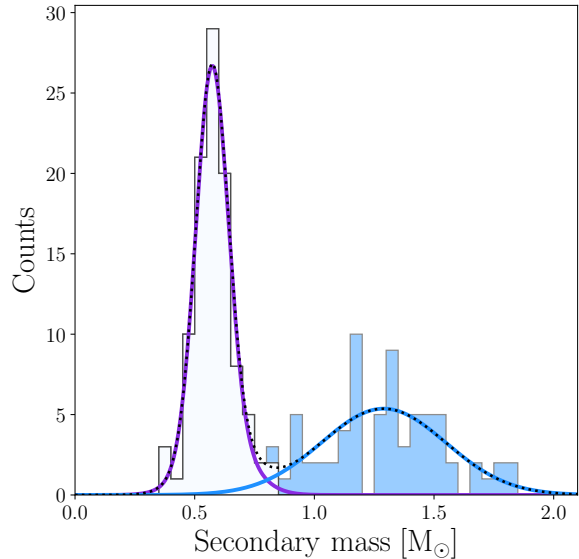


Figure 8. Secondary-mass histogram of the class-III sample. The most prominent peak, at $\sim 0.6 M_{\odot}$ corresponds to WD secondaries in the sample, and another, less prominent peak, is located at $\sim 1.3 M_{\odot}$. We set the upper boundary of the mass axis at $2.1 M_{\odot}$, for clarity. As a result, 8 additional systems with secondary masses larger than $2.4 M_{\odot}$ are not shown. Lines represent the marginal distributions derived from a Gaussian-mixture model that was fitted to the secondary-mass–eccentricity diagram (see Section 5). The overlap between the two classes is small, as only one bin shares points from both classes, with two WDs and one NS.

5 A TENTATIVE DISTINCTION BETWEEN WD AND NS CANDIDATES

The distinction between the WD and the NS in our catalogue is not trivial because some WDs were found to have masses greater than the masses of the least massive NSs (e.g., Martínez et al. 2015; Caiazzo et al. 2021). Furthermore, some compact secondaries with mass typical of NS might be close binaries composed of two white dwarfs. Nevertheless, one might be helped in separating the two populations if some orbital properties of the WD binaries statistically differ from those of the NS binaries.

To explore this possibility, we plot in Figure 7 the orbital eccentricity versus the secondary mass for all objects in our compact-object sample, except for the 8 systems with masses larger than $2.4 M_{\odot}$. The figure suggests two clusters of binaries — one with a typical WD mass of $0.6 M_{\odot}$ and low eccentricity, and the other with a typical NS mass of $1.2 M_{\odot}$ and higher eccentricity.

To tentatively divide the sample into WD and NS candidates, we fitted a 3-component Gaussian mixture model.³ We used two components to describe the distribution of the low-mass circularized systems (‘WD cluster’) and another component for the massive eccentric ones (‘NS cluster’).

³ This was done using Scikit-learn GaussianMixture module.

The WD cluster is described by

$$f_{\text{WD}} \sim 0.78 \mathcal{N} \left(\begin{bmatrix} 0.572 \\ 0.083 \end{bmatrix}, \begin{bmatrix} 0.004 & -0.0006 \\ -0.0006 & 0.001 \end{bmatrix} \right) + \\ 0.22 \mathcal{N} \left(\begin{bmatrix} 0.60 \\ 0.22 \end{bmatrix}, \begin{bmatrix} 0.01 & -0.006 \\ -0.006 & 0.02 \end{bmatrix} \right), \quad (7)$$

where \mathcal{N} represents a normal distribution, its first entry representing the derived expectancy for the secondary mass in Solar units (top) and the eccentricity (bottom), and the second entry is the corresponding covariance matrix. Similarly, the NS cluster is described by

$$f_{\text{NS}} \sim \mathcal{N} \left(\begin{bmatrix} 1.29 \\ 0.43 \end{bmatrix}, \begin{bmatrix} 0.07 & 0.01 \\ 0.01 & 0.05 \end{bmatrix} \right). \quad (8)$$

The odds ratio between the two clusters is 1.42, in favour of the WD cluster.

The central regions of the two clusters are presented as thin purple lines in Figure 7. The points are coloured by their classification: white circles represent the objects in the WD cluster, and the blue circles represent the objects in the NS cluster. The distinction between the two clusters was made according to their cluster-membership probability predicted by the Gaussian mixture model. The 68 targets that have a probability larger than 50% to be members of f_{NS} were labeled as NS cluster members; the 101 targets in the complement set, with probabilities larger than 50% to be members of f_{WD} , were labeled as members of the WD cluster. The 8 BH candidates, with masses larger than $2.4 M_{\odot}$, are not included in any of the two classes.

Gaia DR3 provides quality indicators, such as the significance of the solution and its goodness of fit (GoF). The GoF is normalised such that, for models that are linear in their parameters, its distribution can be approximated by a standard normal distribution. Under this assumption, solutions with $\text{GoF} \gtrsim 3$, for example, should be treated with caution; however, we emphasize that the *Gaia* team considered solutions with GoF of up to 25 as acceptable, given the particular properties of the data and the fitted models (Halbwachs et al. 2022). We did not identify an excess of high GoF targets in the NS cluster members compared to the WD cluster. However, in the case of the BH candidates, 6 out of the 8 targets have values larger than ~ 5 , which might indicate their invalidity.

Figure 8 presents the mass distribution of the secondary masses, overlaid with the marginal probability density function of the Gaussian mixture of Figure 7. The solid purple and blue curves represent the distribution of the WD and NS clusters, respectively, and the combined marginal distribution of the entire sample is shown as a black dotted line.

Out of 177 binaries in the sample, 93 have companions in the mass range of $0.45\text{--}0.75 M_{\odot}$. These systems populate a prominent and narrow histogram peak, centred at $\sim 0.6 M_{\odot}$, which is qualitatively consistent with the observed WD mass distribution (e.g., Tremblay et al. 2016; Hollands et al. 2018). The histogram also shows a broad secondary peak, centred at $\sim 1.3 M_{\odot}$. The high-mass wing of the secondary peak contains 24 systems with companions of $1.4\text{--}2.1 M_{\odot}$, which are probably NSs (but could also be close binaries by themselves composed of two WDs; see the discussion in Mazeh et al. 2022). Additional 48 systems populate the intermediate mass range of $0.75\text{--}1.4 M_{\odot}$, which could either be either NS or massive WDs.

Figures 9 and 10 present the secondary mass and eccentricity versus the orbital period, respectively, for the highly-probable class-III systems in our sample. The points in the figures are coloured according to the tentative mass-eccentricity clustering described above. Figure 9 suggests that (except for two NS cases, Gaia DR3 4482912934572480384 and 1522897482203494784), the NS candi-

dates reported in this study are confined below some upper envelope in the mass-period diagram. Similarly, Figure 10 suggests that an upper envelope also exists in the period-eccentricity plane (except for Gaia DR3 4482912934572480384 and 2574867704662509568). The sample suggests that the NS mass and eccentricity can reach larger values as the orbital period becomes longer.

The CMD location of the compact-object binaries are presented in Figure 11. The figure also shows, for reference, the CMD of the *Gaia* Catalogue of Nearby Stars (GCNS; Smart et al. 2021) for all systems brighter than 15 in *Gaia*'s G band. One can see that all of them have MS primaries, as required by our analysis. As a rule, the binaries occupy the bluer part of the MS stripe, and some less massive white-dwarf binaries are even slightly bluer than the edge of the neighbouring MS stars. This might be due to some short-wavelength contribution from the white-dwarf companions (see, for example, Eyer et al. 2019).

Interestingly, some NS cluster members are also located on the blue side of the MS stripe. One obvious outlier is *Gaia* DR3 2469926638416055168, with an absolute magnitude of ~ 7 and colour index of ~ 0.95 . The binary is eccentric ($e \sim 0.75$), with an orbital period of ~ 580 day. The primary mass is $\sim 0.5 M_{\odot}$, and the companion is of $1.17 \pm 0.14 M_{\odot}$. One possibility is that the companion is a massive WD or a close binary composed of two WDs that was wrongly classified as an NS in our naive tentative Gaussian mixture classification because of the high eccentricity of the wide orbit.

5.1 Incompleteness of the compact object sample

Figure 12 shows the location of the selected binaries on the AMRF–primary-mass plane and illustrates some of the selection biases that affect this sample. The figure shows that all MS-WD binaries have primaries less massive than $\sim 0.7 M_{\odot}$. On the other hand, it seems that MS-NS binaries tend to have primaries more massive than $\sim 0.7 M_{\odot}$. This emerging relationship between the mass of the primary and that of the secondary is probably induced by the triage selection scheme: companions in the WD mass range can be identified as class-III binaries only if the mass of their primary host is sufficiently low (also see Figure 2).

The sample also presents a significant paucity of BH compared to the recent theoretical predictions (e.g., Mashian & Loeb 2017); only 8 systems in the class-III sample have companions more massive than $2.4 M_{\odot}$. Supposedly, very massive non-luminous companions should have been easily detected by *Gaia*. However, as Halbwachs et al. (2022) showed, various properties of *Gaia*'s orbit and sampling yielded spurious orbital solutions, which were often characterized by high mass functions,

$$f_M = \mathcal{A}^3 M_1 > 0.3 M_{\odot}. \quad (9)$$

While Halbwachs et al. (2022) did not explicitly reject systems based on the value of their mass function, it is plausible that many of the BHs and NSs initially detected by *Gaia* were indistinguishable from spurious solutions and consequentially excluded from *Gaia* binary-star database. One possible way of explaining such a bias is by considering the correlation of the parallax error, $\Delta\varpi$, with the photo centre semi-major axis, α_0 . Consequently, the selection imposed on the parallax significance and the orbital period (see Section 3.1) can implicitly impose a selection effect on the total mass of the system. To illustrate this point, we overlaid Figure 12 with three equal- f_M contours. The occurrence rate of the class-III systems appears to be decreasing along the direction perpendicular to these curves, towards high f_M values. While we cannot rule out that this effect is due to the

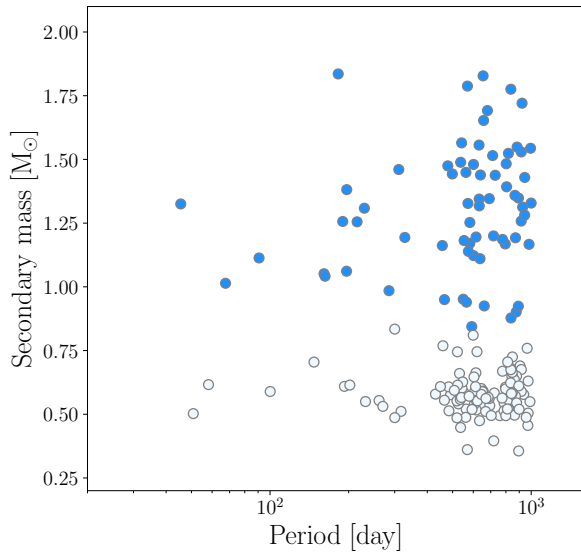


Figure 9. Secondary mass versus orbital period for the class-III sample. Points are coloured by the classification in Figure 7. We set the upper boundary of the mass axis at $2.1 M_{\odot}$, for clarity. As a result, 8 additional systems with secondary masses larger than $2.4 M_{\odot}$ are not shown in the figure.

actual underlying occurrence rates, it is also reasonable to assume that the population of high- f_M companions was significantly depleted in *Gaia* DR3.

The mass distribution of the compact object candidates in our sample is therefore heavily biased. However, while some BH and NS were probably excluded from DR3 and could only be recovered in future data releases, the case of WDs is different. Many WD binaries probably exist in the *Gaia* sample but were identified as class-I/II binaries and consequentially eluded detection. We further discuss the identification of WD secondaries in an accompanying paper.

6 SUMMARY AND DISCUSSION

We have applied the triage analysis of [Shahaf et al. \(2019\)](#) to the recently published sample of *Gaia* astrometric binaries of *NSS*. The analysis divides the astrometric binaries into three classes, class-I — systems with MS secondary, class-II — binaries that are likely to be triple systems, with a close MS binary as the astrometric secondary, and class-III — binaries that probably have a compact-object companion.

The analysis was based on three levels of computation: First, we vetted some of the orbits, based on the relative errors of the Thiele-Innes astrometric parameters, as published by *NSS*, and the recommended selection criteria of [Halbwachs et al. \(2022\)](#). We also rejected binaries with periods longer than 1000 days. Our criteria resulted in 101380 binaries. Second, we adopted a new, conservative, \mathcal{A}_{TR} threshold, based on the MIST stellar evolutionary tracks. Finally, we derived the probability of each binary to be of class-II and class-III, taking into account the uncertainties of the Thiele-Innes parameters and the stellar mass. The main product of this analysis is a catalogue of these astrometric binaries with probabilities to be in each of the classes.

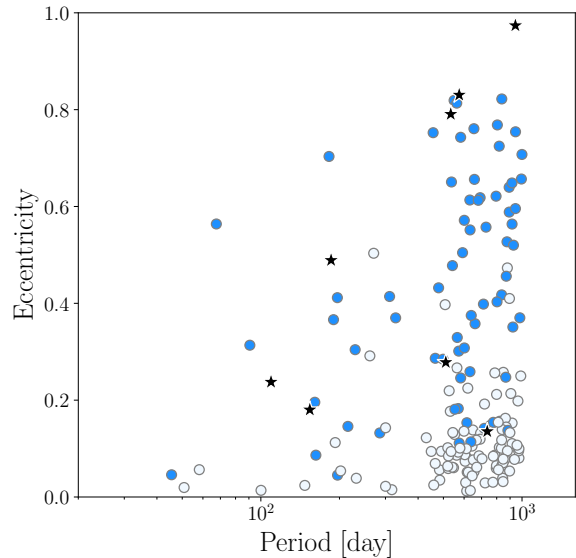


Figure 10. Period-eccentricity diagram of the class-III sample. Points are coloured by the classification in Figure 7. Eight systems, with secondary masses larger than $2.4 M_{\odot}$, are shown as black stars.

Based on the classification probabilities, we constructed a small sample of 177 astrometric binaries that are likely to have compact companions. This sample was chosen such that an expected false-discovery rate is below 10%. For comparison, *NSS* constructed a larger list of 735 binaries. Another catalogue, by [Andrews et al. \(2022\)](#), contained only 24 systems.

The requirements we adopted made our sample of binaries with probable compact objects rather small and incomplete. It is therefore too early to use it to draw conclusions regarding the frequency of binaries with dormant compact companions. However, we already can see some statistical features, plotted in Figures 7–10, that seem real and might be of astrophysical interest.

6.1 WD, NS and BH binaries

The new sample includes eight systems with compact-object masses larger than $2.4 M_{\odot}$, probable binaries with black-hole companions. This classification is somewhat arbitrary, as the borderline between NSs and BHs is not clear. In fact, six of these candidates reside in what was considered a mass gap between the two types of compact objects (e.g., [Kreidberg et al. 2012](#)). However, this gap started to fill up recently by masses measured through gravitational waves (e.g., [Lam et al. 2022](#); [Ye & Fishbach 2022](#)).

The validity of this small BH-candidate sample, however, requires further study. As mentioned in Section 5, most BH candidates have GoF values higher than ~ 5 . One orbital solution, *Gaia* DR3 6588211521163024640, has an exceptionally high eccentricity and an orbital period consistent with ~ 1000 days, which raises suspicions regarding its quality. Validating the orbits of the BH candidates using data sources external to *Gaia* DR3 is crucial. Indeed, several illuminating examples of erroneous orbital solutions or misclassification resulting in false detections of BH-mass companions were recently

Source ID	M_2 (M_\odot)	M_1 (M_\odot)	Period (day)	Eccentricity	s	σ_{TI}
4373465352415301632	12.8(2.6)	1.0	185.77(31)	0.489(74)	13.6	1.2
6281177228434199296	11.9(1.5)	1.0	153.95(36)	0.180(42)	24.3	0.6
3509370326763016704	3.69(24)	0.7	109.392(65)	0.237(16)	76.1	0.2
6802561484797464832	3.08(84)	1.2	574.8(6.2)	0.830(71)	6.8	0.3
3263804373319076480	2.75(50)	1.0	510.7(4.7)	0.278(23)	18.1	2.1
6601396177408279040	2.57(50)	1.0	533.5(2.0)	0.791(43)	10.8	1.1
6328149636482597888	2.45(20)	1.1	736(12)	0.135(36)	89.9	3.8
6588211521163024640	2.41(40)	1.1	943(45)	0.97(12)	10.4	4.2
4482912934572480384	1.84(19)	0.9	182.39(35)	0.703(39)	19.3	0.7
5580526947012630912	1.83(25)	1.2	654.3(4.9)	0.761(40)	12.9	0.1

Table 2. A table of the highly probable class-III systems. The secondary mass of the compact object candidates, derived from the AMRF, appears with its uncertainty. The primary mass, orbital period, eccentricity and significance (denoted s) are taken from the *Gaia* archive. The quadratic mean of the relative error on the Thiele-Innes coefficients denoted σ_{TI} , appears on the rightmost column.

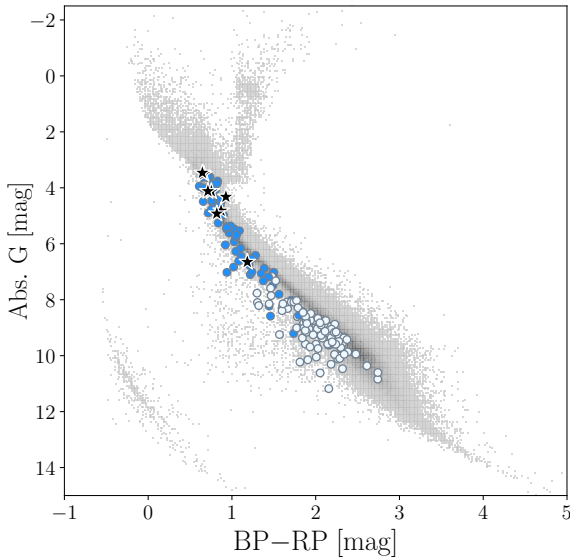


Figure 11. A colour-magnitude diagram showing the *Gaia* G-band absolute magnitude versus the BP-RP colour index for the class-III sample. Points are coloured by their classification in Figure 7. Eight systems with masses larger than $2.4 M_\odot$ are shown as black stars. The grey background shows the *Gaia* Catalogue of Nearby Stars for reference.

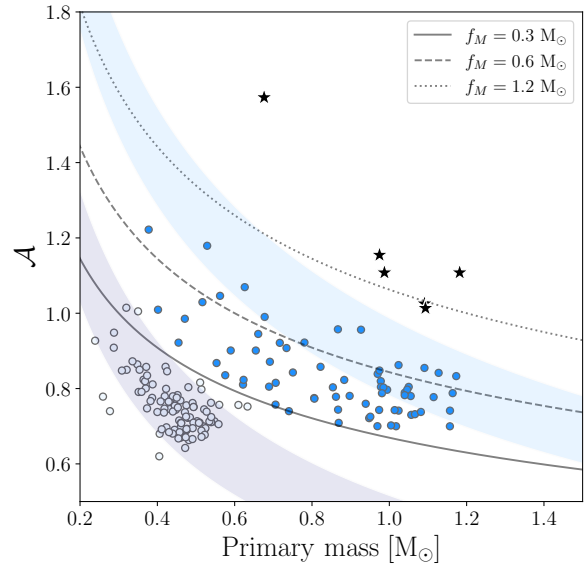


Figure 12. AMRF as a function of primary mass for the class-III sample. Two BH candidates with AMRF values larger than 1.8 are not shown. The remaining six systems with masses larger than $2.4 M_\odot$ appear as black stars. Purple and light-blue stripes represent the locus of typical WDs and NSs (see Figures 2 and 4). Contours of constant mass function, f_M , are plotted as solid, dashed and dotted black lines. Note that axes ranges differ from those of previous Figures.

discussed by [Bashi et al. \(2022\)](#) and [El-Badry & Rix \(2022\)](#) in the context of *Gaia* spectroscopic orbits. However, testing the validity of the astrometric orbits is beyond the scope of this work.

The other 169 systems, with companion masses smaller than $1.85 M_\odot$, are probably mostly WD or NS binaries. We tried to distinguish between the WD and NS by plotting the orbital eccentricity versus the derived compact-object mass. The diagram suggests a clear separation between the WD and the NS binaries. Most of the WD binaries are characterized by small eccentricities of about 0.1 and masses of $0.6 M_\odot$, while the NS binaries display eccentricities of about 0.4 and masses of $1.3 M_\odot$. The latter feature might be due to the natal kicks that accompany the NSs formation ([Hansen & Phinney 1997](#); [Igoshev & Perets 2019](#)), although their underlying physical mecha-

nism is a matter of ongoing research ([Atri et al. 2019](#); [Callister et al. 2021](#); [Willcox et al. 2021](#); [Andrews & Kalogera 2022](#)).

As a population, the detected binaries in the NS cluster carry the potential of probing the margins of the natal kick velocity distribution that is assumed to be associated with the NS formation. With orbital periods on the order of a few years and eccentricities below ~ 0.8 , these binaries probably represent the products of processes that, while strong enough to induce eccentricity to the orbit, could not disrupt the binary entirely (e.g., [Pfahl et al. 2002](#); [van den Heuvel 2007](#); [Beniamini & Piran 2016](#); [Tauris et al. 2017](#)).

As opposed to the NS candidates, most binaries in the WD cluster have relatively circular orbits, regardless of their orbital periods

(see Figures 7 and 10). However, it is evident that many have small eccentricities (see Section 5). WDs are expected to be in highly circularized orbits due to the tidal interaction between the WD progenitors and their MS companion, and therefore our result could be of interest (Zahn 1977; Izzard et al. 2010; Van der Swaelmen et al. 2017; Jorissen et al. 2019). However, it is too early to determine whether those small eccentricities are significant. One could claim, for example, that this is not an inherent property of the sample, as it could originate from the fitting procedure or a sample selection (see the caveats discussion below).

As pointed out above, the most striking feature of Figures 9 is the concentration of the binaries in a period range of about 400–1000 days. One needs to check whether this results from an observational bias, as the longer the period, the larger the semi-major axis is. Similarly, the figures suggest that upper envelopes of the NS distributions with larger mass and eccentricity for orbits with longer periods have surfaced. If this is not another result of an observational bias, it could be the result of the natal kicks discussed above, which might produce statistical dependence between the resulting period and the NS mass and orbital eccentricity (Hills 1983; Brandt & Podsiadlowski 1995; Kalogera 1996; Dewi et al. 2005).

The mass distribution of the WD and NS class-III sample is presented in Figure 8 (also see figure 36 of *NSS*). The advantage of a sample of astrometric binaries with compact companions is the ability to dynamically derive the secondary mass of each binary, which depends only on the primary and orbital elements, provided the secondary is non-luminous. The derived masses of WD, for example, do not depend on evolutionary tracks nor on spectral analysis (e.g., Bergeron et al. 2019; Torres et al. 2021; Fantin et al. 2021; Heintz et al. 2022).

The secondary-mass histogram presents a sharp peak at $\sim 0.6 M_{\odot}$, with a width of $\sim 0.1 M_{\odot}$, similar to the peak found in the distribution of the white dwarf in the solar neighbourhood by Tremblay et al. (2016) and Hollands et al. (2018). We, therefore, can assume that the peak of Figure 8 does reflect the masses of a large sample of white-dwarf secondaries (see also *NSS*). It seems as if the WD distribution reported by Hollands et al. (2018) is wider than the one of Figure 8. One might wonder if this is because of the more precise determination of the white-dwarf companion mass by dynamical techniques. In any case, it is also possible that the proximity of the companion through the last evolutionary phases leading to the production of WDs might modify the mass of the end product (e.g., Toonen et al. 2014).

The mass distribution of Figure 8 includes a wide ‘wing’ to the right of the sharp peak, centered around $\sim 1.3 M_{\odot}$, that we identified as NSs, consistent with their expected masses (e.g., Lattimer & Steiner 2014; Özel & Freire 2016). The mass-eccentricity diagram suggests that within the period range probed by *Gaia* the WD and NS mass distributions only slightly overlap — compact companions more massive than $\sim 1 M_{\odot}$ are likely to be NS. This observation stands in contrast with the recent analysis of the *Gaia* EDR3 catalog (Gentile Fusillo et al. 2021) which argues that the mass distribution of white dwarfs in the solar neighborhood has a long tail extending to $1.2 M_{\odot}$ and even higher. However, the latter distribution was derived for single WDs, for which the massive tail might reflect the result of two merging WDs (Kilic et al. 2021; Miller et al. 2022; Fleury et al. 2022a,b). Our tentative separation, on the other hand, is based on the masses of compact companions, for which the binarity did not allow the merging of two WDs in the close proximity of the optical star. Such a distinction might have obvious implications for classifying non-interacting compact objects (see, for example, Mazeh et al. 2022).

Many binaries with compact secondaries were previously known,

either as cataclysmic variables (e.g., Robinson 1976; Knigge et al. 2011), X-ray binaries (e.g., Paul 2017) or some binary pulsars (e.g., Manchester 2017). Most of those (except Be/X-ray binaries and a few pulsars) reside in short-period orbits, on the order of hours and days. Most of them were discovered by the luminosity of the compact objects or the accretion disks around them, which are fueled by mass transfer from the optical companion or the rotational energy of the compact object (but see Shenar et al. 2022a,b). The companions sampled here are all dormant, and their identification is based on the astrometric motion of the optical star only. Their orbital periods are on the order of a year, allowing a look into another range of periods of the compact-object binaries (see, for example, Saracino et al. 2022; but also El-Badry & Burdge 2022).

6.2 Caveats

There are several caveats to our analysis, which we briefly address below.

Foremost, despite our cautious approach, the validity of the orbits is still in doubt. The sample of astrometric binaries detected by *Gaia* probably includes some false discoveries, as any other database would. However, as was shown by Halbwachs et al. (2022), the spurious orbital solutions detected by *Gaia* are often characterized by high mass functions. As a result, samples of massive non-luminous companions found in the *NSS* catalogue should be treated with some caution. Furthermore, the very nature of the *Gaia* astrometric 1-D measurements (Gaia Collaboration et al. 2016; Pourbaix et al. 2022), the relatively small number of observations (*NSS*), and the fact that DR3 does not include the individual measurements imply that unambiguous detection of extremely rare systems based DR3 data alone is challenging. Therefore, the orbits in our sample should be validated by radial-velocity (RV) follow-up observations, for example. The amplitude of the expected modulation should be on the order of 30 km/s, and therefore a few observations close to the quadrature phases, when the RVs get their extreme values, should suffice.

Second, our analysis relies on *Gaia*’s reported masses, along with their uncertainty estimates. It will be useful to consider external estimates for the stellar parameters via spectroscopy from the LAMOST (Cui et al. 2012) or GALAH (Buder et al. 2021) surveys, for example.

Third, we emphasize that our tentative Gaussian mixture classification, separating between WD and NS candidates, is only of statistical nature. It does not account for uncertainties in the data, the prior knowledge of the physical properties, nor any additional data apart from their mass and eccentricity. To draw more specific conclusions, one might also wish to consider, for example, the spectral energy distribution, chemical composition, and Galactic trajectory of these binaries.

Looking into the future, when the next *Gaia* release comes, the number of observations gets larger, and the whole astrometric data is released. Furthermore, the time span of the observations gets longer, and the sample of binaries grows substantially. We will then be able to estimate the validity of the orbits and the observational threshold for astrometric detection, deriving the statistical features of the compact-object binaries, particularly the frequency of the compact-object binaries as a function of the orbital period.

ACKNOWLEDGEMENTS

We thank Na’ama Hallakoun, Shany Danieli and Boaz Katz for their insightful suggestions and valuable comments. The research of SS

is supported by a Benoziyo prize postdoctoral fellowship. This research was supported by Grant No. 2016069 of the United States-Israel Binational Science Foundation (BSF) and by Grant No. I-1498-303.7/2019 of the German-Israeli Foundation for Scientific Research and Development (GIF) to TM and HWR.

This work has made use of data from the European Space Agency (ESA) mission *Gaia* (<http://www.cosmos.esa.int/gaia>), processed by the Gaia Data Processing and Analysis Consortium (DPAC, <http://www.cosmos.esa.int/web/gaia/dpac/consortium>). Funding for the DPAC has been provided by national institutions, in particular the institutions participating in the *Gaia* Multilateral Agreement.

This work made use of **ArtPop**, a Python package for synthesizing stellar populations and simulating realistic images of stellar systems (Greco & Danieli 2021); the MIST isochrone grids (Paxton et al. 2011, 2013, 2015; Choi et al. 2016; Dotter 2016); The **WD models** package for WD photometry to physical parameters; **catsHTM**, a tool for fast accessing and cross-matching large astronomical catalogs (Soumagnac & Ofek 2018); **Astropy**, a community-developed core Python package for Astronomy (Astropy Collaboration et al. 2013, 2018); **matplotlib** (Hunter 2007); **numpy** (Oliphant 2006; Van der Walt et al. 2011); **scipy** (Virtanen et al. 2020); and **Scikit-learn** (Pedregosa et al. 2011).

DATA AVAILABILITY

All data underlying this research are publicly available. The classification tables will be made available as supplementary material upon publication.

REFERENCES

- Andrae R., et al., 2022, arXiv e-prints, p. [arXiv:2206.06138](https://arxiv.org/abs/2206.06138)
- Andrew S., Penoyre Z., Belokurov V., Evans N. W., Oh S., 2022, arXiv e-prints, p. [arXiv:2206.04392](https://arxiv.org/abs/2206.04392)
- Andrews J. J., Kalogera V., 2022, *ApJ*, **930**, 159
- Andrews J. J., Breivik K., Chatterjee S., 2019, *ApJ*, **886**, 68
- Andrews J. J., Taggart K., Foley R., 2022, arXiv e-prints, p. [arXiv:2207.00680](https://arxiv.org/abs/2207.00680)
- Astropy Collaboration et al., 2013, *A&A*, **558**, A33
- Astropy Collaboration et al., 2018, *AJ*, **156**, 123
- Atri P., et al., 2019, *Monthly Notices of the Royal Astronomical Society*, **489**, 3116
- Babusiaux C., et al., 2022, arXiv e-prints, p. [arXiv:2206.05989](https://arxiv.org/abs/2206.05989)
- Bashi D., Shahaf S., Mazeh T., Faigler S., Dong S., El-Badry K., Rix H.-W., Jorissen A., 2022, arXiv e-prints, p. [arXiv:2207.08832](https://arxiv.org/abs/2207.08832)
- Beniamini P., Piran T., 2016, *MNRAS*, **456**, 4089
- Beniamini Y., Hochberg Y., 1995, *Journal of the Royal statistical society: series B (Methodological)*, **57**, 289
- Bergeron P., Dufour P., Fontaine G., Coutu S., Blouin S., Genest-Beaulieu C., Bédard A., Rolland B., 2019, *ApJ*, **876**, 67
- Brandt N., Podsiadlowski P., 1995, *MNRAS*, **274**, 461
- Breivik K., Chatterjee S., Larson S. L., 2017, *ApJ*, **850**, L13
- Buder S., et al., 2021, *MNRAS*, **506**, 150
- Caiazzo I., et al., 2021, *Nature*, **595**, 39
- Callister T. A., Farr W. M., Renzo M., 2021, *The Astrophysical Journal*, **920**, 157
- Cerda-Duran P., Elias-Rosa N., 2018, in Rezzolla L., Pizzochero P., Jones D. I., Rea N., Vidiña I., eds, *Astrophysics and Space Science Library* Vol. 457, *Astrophysics and Space Science Library*. p. 1 ([arXiv:1806.07267](https://arxiv.org/abs/1806.07267)), doi:[10.1007/978-3-319-97616-7_1](https://doi.org/10.1007/978-3-319-97616-7_1)
- Chawla C., Chatterjee S., Breivik K., Moorthy C. K., Andrews J. J., Sanderson R. E., 2022, *ApJ*, **931**, 107
- Choi J., Dotter A., Conroy C., Cantiello M., Paxton B., Johnson B. D., 2016, *ApJ*, **823**, 102
- Creevey O. L., et al., 2022, arXiv e-prints, p. [arXiv:2206.05864](https://arxiv.org/abs/2206.05864)
- Cui X.-Q., et al., 2012, *RAA*, **12**, 1197
- Davison A. C., Hinkley D. V., 1997, *Bootstrap Methods and their Application*. Cambridge Series in Statistical and Probabilistic Mathematics, Cambridge University Press, doi:[10.1017/CBO9780511802843](https://doi.org/10.1017/CBO9780511802843)
- Dewi J. D. M., Podsiadlowski P., Pols O. R., 2005, *MNRAS*, **363**, L71
- Dotter A., 2016, *ApJS*, **222**, 8
- El-Badry K., Burdge K. B., 2022, *MNRAS*, **511**, 24
- El-Badry K., Rix H.-W., 2022, *MNRAS*,
- Eyer L., et al., 2019, *A&A*, **623**, A110
- Fantini N. J., et al., 2021, *ApJ*, **913**, 30
- Fleury L., Caiazzo I., Heyl J., 2022a, arXiv e-prints, p. [arXiv:2205.01015](https://arxiv.org/abs/2205.01015)
- Fleury L., Caiazzo I., Heyl J., 2022b, *MNRAS*, **511**, 5984
- Fryer C. L., Belczynski K., Wiktorowicz G., Dominik M., Kalogera V., Holz D. E., 2012, *ApJ*, **749**, 91
- Gaia Collaboration et al., 2016, *A&A*, **595**, A1
- Gaia Collaboration et al., 2022, arXiv e-prints, p. [arXiv:2206.05595](https://arxiv.org/abs/2206.05595)
- Gentile Fusillo N. P., et al., 2021, *MNRAS*, **508**, 3877
- Greco J. P., Danieli S., 2021, arXiv e-prints, p. [arXiv:2109.13943](https://arxiv.org/abs/2109.13943)
- Halbwachs J.-L., et al., 2022, arXiv e-prints, p. [arXiv:2206.05726](https://arxiv.org/abs/2206.05726)
- Hansen B. M. S., Phinney E. S., 1997, *Monthly Notices of the Royal Astronomical Society*, **291**, 569
- Heacox W. D., 1995, *AJ*, **109**, 2670
- Heger A., Fryer C. L., Woosley S. E., Langer N., Hartmann D. H., 2003, *ApJ*, **591**, 288
- Heintz T. M., Hermes J. J., El-Badry K., Walsh C., van Saders J. L., Fields C. E., Koester D., 2022, *ApJ*, **934**, 148
- Hills J. G., 1983, *ApJ*, **267**, 322
- Hollands M. A., Tremblay P. E., Gänsicke B. T., Gentile-Fusillo N. P., Toonen S., 2018, *MNRAS*, **480**, 3942
- Hunter J. D., 2007, *Computing In Science & Engineering*, **9**, 90
- Igoshev A. P., Perets H. B., 2019, *Monthly Notices of the Royal Astronomical Society*, **486**, 4098
- Izzard R. G., Dermine T., Church R. P., 2010, *A&A*, **523**, A10
- Janssens S., et al., 2022, *A&A*, **658**, A129
- Jorissen A., Frankowski A., 2008, in Pellegrini P., Daflon S., Alcaniz J. S., Telles E., eds, *American Institute of Physics Conference Series* Vol. 1057, *Graduate School in Astronomy: XII Special Courses at the National Observatory of Rio de Janeiro*. pp 1–55 ([arXiv:0804.3720](https://arxiv.org/abs/0804.3720)), doi:[10.1063/1.2999998](https://doi.org/10.1063/1.2999998)
- Jorissen A., Boffin H. M. J., Karinkuzhi D., Van Eck S., Escorza A., Shetye S., Van Winckel H., 2019, *A&A*, **626**, A127
- Kalogera V., 1996, *ApJ*, **471**, 352
- Kilic M., Bergeron P., Blouin S., Bédard A., 2021, *MNRAS*, **503**, 5397
- Knigge C., Baraffe I., Patterson J., 2011, *ApJS*, **194**, 28
- Kreidberg L., Bailyn C. D., Farr W. M., Kalogera V., 2012, *ApJ*, **757**, 36
- Lam C. Y., et al., 2022, *ApJ*, **933**, L23
- Lattimer J. M., Steiner A. W., 2014, *ApJ*, **784**, 123
- Manchester R. N., 2017, *Journal of Astrophysics and Astronomy*, **38**, 42
- Martinez J. G., et al., 2015, *ApJ*, **812**, 143
- Mashian N., Loeb A., 2017, *MNRAS*, **470**, 2611
- Mazeh T., et al., 2022, arXiv e-prints, p. [arXiv:2206.11270](https://arxiv.org/abs/2206.11270)
- Miller D. R., Caiazzo I., Heyl J., Richer H. B., Tremblay P.-E., 2022, *ApJ*, **926**, L24
- Morrell S., Naylor T., 2019, *MNRAS*, **489**, 2615
- Oliphant T., 2006, *NumPy: A guide to NumPy*, USA: Trelgol Publishing, <http://www.numpy.org/>
- Özel F., Freire P., 2016, *ARA&A*, **54**, 401
- Paul B., 2017, *Journal of Astrophysics and Astronomy*, **38**, 39
- Paxton B., Bildsten L., Dotter A., Herwig F., Lesaffre P., Timmes F., 2011, *ApJS*, **192**, 3
- Paxton B., et al., 2013, *ApJS*, **208**, 4
- Paxton B., et al., 2015, *ApJS*, **220**, 15
- Pecaut M. J., Mamajek E. E., 2013, *ApJS*, **208**, 9
- Pedregosa F., et al., 2011, *Journal of Machine Learning Research*, **12**, 2825
- Pfahl E., Rappaport S., Podsiadlowski P., Spruit H., 2002, *ApJ*, **574**, 364
- Pourbaix D., et al., 2022, *Gaia DR3 documentation Chapter 7: Non-single*

- stars, Gaia DR3 documentation, European Space Agency; Gaia Data Processing and Analysis Consortium.
- Robinson E. L., 1976, *ARA&A*, 14, 119
- Saracino S., et al., 2022, *MNRAS*, 511, 2914
- Shahaf S., Mazeh T., Faigler S., 2017, *MNRAS*, 472, 4497
- Shahaf S., Mazeh T., Faigler S., Holl B., 2019, *MNRAS*, 487, 5610
- Shenar T., et al., 2022a, *Nature Astronomy*,
- Shenar T., et al., 2022b, arXiv e-prints, p. arXiv:2207.07674
- Smart R. L., et al., 2021, *A&A*, 649, A6
- Soumagnac M. T., Ofek E. O., 2018, *PASP*, 130, 075002
- Tauris T. M., et al., 2017, *ApJ*, 846, 170
- Toonen S., Claeys J. S. W., Mennekens N., Ruiter A. J., 2014, *A&A*, 562, A14
- Torres S., Rebassa-Mansergas A., Camisassa M. E., Raddi R., 2021, *MNRAS*, 502, 1753
- Tremblay P. E., Cummings J., Kalirai J. S., Gänsicke B. T., Gentile-Fusillo N., Raddi R., 2016, *MNRAS*, 461, 2100
- Van der Swaelmen M., Boffin H. M. J., Jorissen A., Van Eck S., 2017, *A&A*, 597, A68
- Virtanen P., et al., 2020, *Nature Methods*, 17, 261
- van der Walt S., Colbert S. C., Varoquaux G., 2011, *Computing in Science Engineering*, 13, 22
- Willcox R., Mandel I., Thrane E., Deller A., Stevenson S., Vigna-Gómez A., 2021, *The Astrophysical Journal Letters*, 920, L37
- Yamaguchi M. S., Kawanaka N., Bulik T., Piran T., 2018, *ApJ*, 861, 21
- Ye C., Fishbach M., 2022, arXiv e-prints, p. arXiv:2202.05164
- Zahn J. P., 1977, *A&A*, 57, 383
- van den Heuvel E. P. J., 2007, in di Salvo T., Israel G. L., Piersant L., Burderi L., Matt G., Tornambe A., Menna M. T., eds, American Institute of Physics Conference Series Vol. 924, *The Multicolored Landscape of Compact Objects and Their Explosive Origins*. pp 598–606 (arXiv:0704.1215), doi:10.1063/1.2774916

APPENDIX A: MINIMAL MASS-RATIO FROM THE AMRF

A lower estimate for the mass ratio is obtained by assuming that the secondary companion is non-luminous, namely, plugging $S = 0$ into equation (2). Under this assumption, the AMRF is a function of the mass ratio alone,

$$\mathcal{A}^3 = \frac{q^3}{(1+q)^2}, \quad (\text{A1})$$

and the minimal mass ratio, q_{\min} is, therefore, a root of the polynomial

$$P(q; A) = \mathcal{A}^{-3}q^3 - q^2 - 2q - 1. \quad (\text{A2})$$

Since \mathcal{A} is a finite positive number the minimal mass ratio is unique and can be obtained analytically (e.g., Heacox 1995; Shahaf et al. 2017). The corresponding minimal secondary mass, i.e., the mass of the companion assuming that it does not emit light, is given by

$$M_{2,\min} = q_{\min} \cdot M_1. \quad (\text{A3})$$

APPENDIX B: DERIVING THE LIMITING \mathcal{A}_{TR} CURVE

In Section 2.2 we show that the shape of \mathcal{A}_{MS} and \mathcal{A}_{TR} depends on the age and composition of the stars in the binary system. In light of this claim, a plausible course of action would be to classify each binary while considering its particular age, iron abundance, and corresponding uncertainty estimates.

However, we note that the FLAME stellar ages tend to have large uncertainties (Creveley et al. 2022; Babusiaux et al. 2022) and the GSP-phot metallicity are probably biased and require further calibration (Andrae et al. 2022). Furthermore, these values are provided

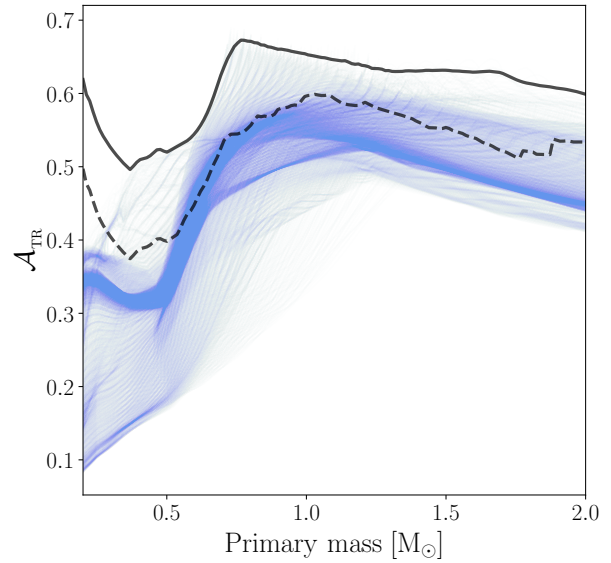


Figure B1. The limiting AMRF value, \mathcal{A}_{TR} versus the mass of the primary star. An ensemble of models generated from the grid of MIST isochrones appears in light blue. The ‘global’ limit we adopted is plotted as a solid black line. For reference, we also show the limiting curve used by the NSS team as a dashed black line.

by *Gaia* only to about half of the sample of astrometric binaries. As a result, and after attempting to incorporate these values, we concluded that the use of individual age and metallicity estimates is not efficient. Instead, we opted to derive a ‘global’ limiting curve that can provide a conservative estimate for the values for the classification, even when the age and composition are not well constrained.

To do so, we generated a set of \mathcal{A}_{MS} and \mathcal{A}_{TR} curves, spanning from 7 to 10.2 in $\log(\text{Age}/\text{yr})$ and -3 to 0.5 in $[\text{Fe}/\text{H}]$. The spacing in both grids is 0.05 dex. Based on this set of limiting values, we generated a new limiting curve that follows the outer envelope of all curves in our grid. To do so, we used the 99.9 percentile of all curves for a given mass value and smoothed the resulting envelope with a moving average with a width of $\sim 0.1 M_{\odot}$.

Theoretical models are known to be prone to estimate the radii of M-dwarfs inaccurately (e.g., Morrell & Naylor 2019). Therefore, for primary stars less massive than $0.5 M_{\odot}$, instead of using the curve based on the upper envelope of the theoretical models, we used the one based on the Pecaut & Mamajek (2013) MLR. We added a positive constant to this low-mass limiting curve to ensure that the final resulting curve is continuous. The resulting limiting curve is plotted, along with all the models used in our ensemble, in Figure B1.

This paper has been typeset from a $\text{\TeX}/\text{\LaTeX}$ file prepared by the author.